Nanoscale

Accepted Manuscript

This article can be cited before page numbers have been issued, to do this please use: G. Bucci, V. G. Dubrovskii, V. Zannier, F. Beltram and L. Sorba, *Nanoscale*, 2025, DOI: 10.1039/D5NR02409A.

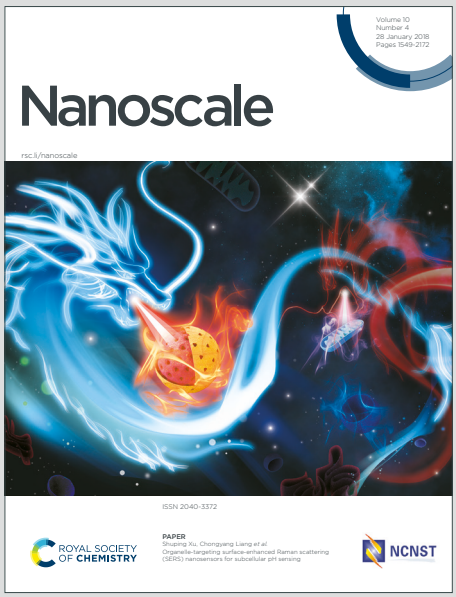

ROYAL SOCIETY OF CHEMISTRY

rsc.li/nanoscale

View Article Online
DOI: 10.1039/D5NR02409A

ARTICLE

The role of composition and diameter on the crystal purity of $InAs_xP_{1-x}$ nanowires

Received 00th January 20xx,
Accepted 00th January 20xx

DOI: 10.1039/x0xx00000x

Giada Bucci,[a] Vladimir G. Dubrovskii[b], Valentina Zannier*[a], Fabio Beltram[a] and Lucia Sorba[a]

Ternary $InAs_xP_{1-x}$ nanowires are widely considered as promising building blocks for fundamental studies and applications in nano- and optoelectronics. However, it is admittedly challenging to maintain the necessary control over the crystal purity of nanowires. Furthermore, the crystal phase trends in ternary III-V nanowires remain generally unknown. In this work, we present wurtzite $InAs_xP_{1-x}$ nanowires with different compositions x, ranging from 0 to 0.54, grown via chemical beam epitaxy on InP(111)B substrates using Au colloidal catalysts of different diameters. Transmission electron microscopy studies reveal that pure wurtzite phase of the nanowires requires larger InAs fractions x for larger diameters of Au colloids (in particular, $x = 0.36$ for 20 nm diameter and $x = 0.54$ for 30 nm diameter Au colloids). We develop a model for the critical composition of thin vapor-liquid-solid III-V ternary nanowires x_c corresponing to the transition from a polytypic structure at $x < x_c$ to pure wurtzite structure at $x > x_c$. For $InAs_xP_{1-x}$ material, the critical composition increases with the nanowire diameter, which explains our experimental findings. These results shed more light on the composition and diameter dependent polytypism, offering valuable insights for the design and crystal phase control of $InAs_xP_{1-x}$ and other III-V ternary nanowires.

1. Introduction

III-V semiconductor nanowires (NWs) have extensively been studied due to their unique structural, electronic, and optical properties. Thanks to their high aspect ratio, NWs can relax strain radially, enabling the integration of highly lattice-mismatched materials without introducing dislocations. This feature enables greater flexibility in realizing NW heterostructures comprised of dissimilar materials and bandgap engineering in such heterostructures compared to epi-layers[1]. NWs are often synthesized via a metal-assisted vapor-liquid-solid (VLS) growth method. By tuning the growth conditions, substrate orientation, catalyst material and NW diameter, both hexagonal wurtzite (WZ) and cubic zincblende (ZB) crystal phases can be obtained in III-V NWs.[2] Pure WZ phase is never observed in bulk III-V materials, but easily achieved in binary III-V NWs. This crystal phase is of great interest due to several intriguing properties, like the possibility of realizing the vanishing fine-structure splitting in WZ quantum dots (QDs)[3] or obtaining direct band gap structure of GaP, AlGaAs and some other III-V materials[4,5]. Recently, significant efforts have been put on synthesis and investigations of III-V ternary NWs, which offer promising applications due to their bandgap tunability and the emergence of novel properties. Among ternary alloys, $InAs_xP_{1-x}$ has attracted particular interest for its potential in a wide range of technologies. This material exhibits excellent piezoelectric properties[6,7] and tunable direct band gap ranging from 0.351 eV to 1.351 eV[8], making it highly suitable for applications in optoelectronics, quantum computing, and quantum information technologies. Additionally, low effective mass and high electron mobility in $InAs_xP_{1-x}$ is attractive for the realization of high-performance electronic devices. Significant research efforts have focused on the synthesis of $InAs_xP_{1-x}$ quantum dots in InP NWs, which are promising for single photon emission[9,10].

Notably, improved optical properties have been observed when these QDs are inserted into an $InAs_xP_{1-x}$ segment with a reduced InAs fraction[11], a strategy that requires precise control over the formation of ternary NWs. To date, the ternary alloy engineering in NWs have mainly concentrated on the compositional control[8,12,13]. However, the defect-free structure of $InAs_xP_{1-x}$ is absolutely required for all the envisioned applications, because structural defects are known to degrade both electronic and optical performance of the material. Due to the different band structure of the WZ and ZB phases, their intermix in the same NW introduces electron and phonon scattering at the interfaces and the formation of charge traps[14–16] . Avoiding polytypism remains challenging even in binary InP and InAs NWs, since the NWs growth along the <111> direction promotes the formation of stacking faults due to the small energy difference between the WZ and ZB stacking in this direction.[17] The crystal phase purity in both InP and InAs NWs has been shown to depend on several growth parameters including growth temperature, V/III ratio, total precursor fluxes and diameter. The latter dependence has been ascribed to the Gibbs-Thomson effect[18]. Defect-free WZ InP NWs have been demonstrated, to the best of our knowledge, only in NWs with very small diameters (up to 20 nm)[16]. In contrast, InAs NWs tend to form in the WZ crystal phase even at larger diameters, although the diameter dependence has also been reported for this material[18] . Here, we present a study on the crystal phase purity of ternary $InAs_xP_{1-x}$ NWs as a function of the NW diameter and chemical composition. We find the existence of a critical

[a] NEST Scuola Normale Superiore of Pisa and Istituto Nanoscienze Consiglio Nazionale delle Ricerche (CNR), 56127, Pisa, Italy.
[b] Faculty of Physics, St. Petersburg State University, Universitetskaya Embankment 7-9, 199034 St. Petersburg, Russia

composition, above which the $InAs_xP_{1-x}$ NWs are pure WZ. This critical composition increases with the NW diameter.

In general, the crystal phase trends in VLS III-V ternary NWs were not systematically quantified and remain largely unknown. Consequently, we develop a semi-quantitative model for the composition and diameter dependent polytypism in such NWs and show that the percentage of the WZ phase is generally a function of two variables, the NW diameter $\boldsymbol{2R}$ and composition, represented by the InAs fraction in the ternary alloy $\boldsymbol{x}$. The diameter dependence originates from the contributions of edges separating the NW facets into the overall surface energy balance, which become important for thin NWs. Hence, the critical composition $\boldsymbol{x_c}$ in VLS III-V ternary NWs, corresponding to the transition from a polytypic WZ/ZB intermix at $\boldsymbol{x < x_c}$ to pure WZ structure at $\boldsymbol{x > x_c}$, depends on the NW diameter. For $InAs_xP_{1-x}$ material, the critical composition increases with the NW diameter, which explains the data. This work extends the approaches originally developed for binary systems to a more complex case of VLS III-V ternary NWs, providing insights into the interplay between diameter, composition and crystal phase. To the best of our knowledge, we demonstrate for the first time a diameter-dependent critical composition required to achieve phase-pure ternary wurtzite NWs. The results should be useful from a general perspective and for the crystal phase engineering in thin $InAs_xP_{1-x}$ NWs, and can be translated to other material systems.

2. Results and discussion

Defect-free WZ InP NWs grown from 10 nm diameter Au colloids have already been reported in the literature[19]. At this diameter, the WZ crystal phase is energetically preferred also for InAs NWs.[18] To explore the dependence of the crystal phase on the NW diameter and composition, we decide to focus on larger diameters, where a mixed ZB/WZ crystal phase typically occurs in both binary NWs[18,20,21]. Different samples were grown using Au colloidal nanoparticles (NPs) of 20 nm and 30 nm diameter, which resulted in the NW diameters of ~25 nm and up to ~45 nm, respectively. All the NW samples investigated in this work were grown with the same procedure. After heating the InP (111)B substrate to 400 ± 10 °C under a Tert-butyl phosphine (TBP) line pressure of 1 Torr, the NW growth was initiated by introducing trimethylindium (TMIn), TBP and, when required, tert-butyl arsine (TBAs). The growth was carried out for 120 minutes to obtain NWs with lengths of 1090 ± 200 nm for 20 nm diameter colloids and 330 ± 30 nm for 30 nm diameter colloids.

Figure 1 shows the results for the NWs grown from 20 nm diameter NPs. Additional TEM images are reported in section S1 of the supporting information. In panel (a), 45°-tilted view SEM image shows an ensemble of binary InP NWs grown using TMIn and TBP precursor line pressures of 0.30 Torr and 1.05 Torr, respectively. Two different NW morphologies are highlighted with orange and green boxes. The former, referred to as "type 1" in the following, is characterized by the enhanced radial growth, indicated by red arrow in Figure 1(a). This enhancement has previously been reported in the literature[22], and is attributed to the NW sections with a high density of stacking faults. This is also confirmed for our sample. Panel (b) of Figure 1 presents a high-resolution transmission electron microscopy (HRTEM) image of such NW, showing the presence of crystal defects. In contrast, the latter type of NW, labelled as "type 2" in the following, displays nearly untapered morphology with no significant radial growth or bulges along its length. This morphology is characterized by a low stacking fault density or even fully defect-free WZ crystal phase, as demonstrated by the HRTEM image in Figure 1(c).

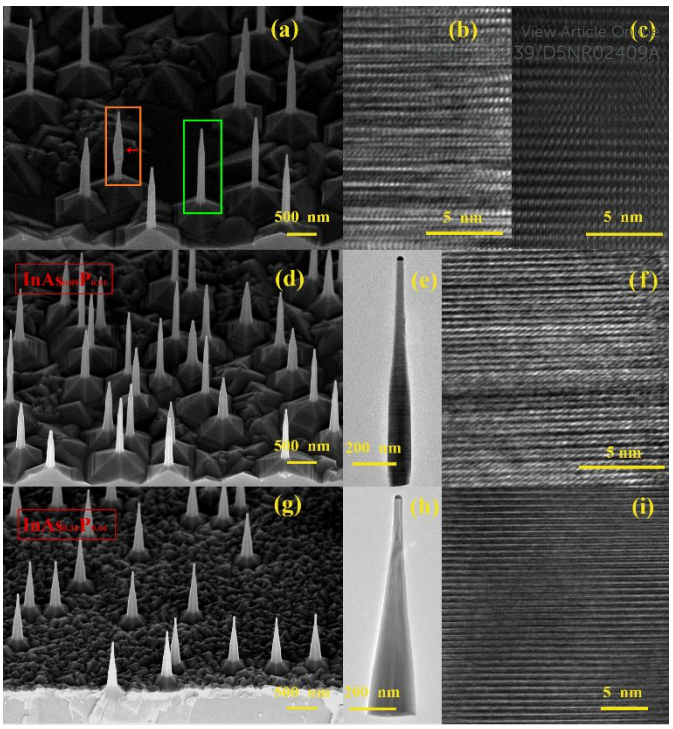

Figure 1 (a) 45°-tilted SEM image of InP NWs grown from 20 nm Au NPs. Orange and green boxes highlight the NWs of type 1 (tapered morphology and high stacking fault density) and type 2 (untapered morphology and nearly pure WZ phase), respectively. (b) Representative HRTEM image of type 1 NW, showing the presence of high density crystal defects; (c) representative HRTEM image of type 2 NW, showing a good crystal quality in the WZ phase for this morphology; (d) 45°-tilted SEM image of $InAs_{0.09}P_{0.91}$ NW ensemble, with its TEM in panel (e) and the HRTEM image in panel (f), showing the presence of stacking faults also in this sample; (g) 45°-tilted SEM image of $InAs_{0.36}P_{0.64}$ NW ensemble, with its TEM in panel (h) and the HRTEM image in panel (i), showing defect-free WZ crystal phase of excellent quality.

To identify the optimal growth conditions for obtaining pure WZ binary InP NWs with untapered geometry, we studied the growth under different V/III ratio values by varying the TBP line pressure from 0.50 Torr to 1.50 Torr and keeping the TMIn pressure constant at 0.30 Torr. In all cases, we obtained NW ensembles with both morphologies. Hence, we selected the growth condition that minimized the occurrence of type 1 NWs with high stacking fault density. Based on this criterion, the optimal TBP line pressures was identified at 1.05 Torr (i.e., the sample in Figure 1(a)). Under these precursor fluxes, approximately 42% of the NWs exhibit the unwanted type 1 morphology, while the remaining portion corresponds to type 2 morphology. A total of 50 NWs have been analyzed for the percentage estimation. After selecting the best conditions for binary InP NWs of this diameter, we have investigated the growth of $InAs_xP_{1-x}$ ternary NWs. To evaluate the effect of As incorporation on the crystal purity of the NWs, we grew a series of samples at the same temperature of 400 °C keeping the TMIn line pressure at 0.30 Torr, and a constant total group-V line pressure (TBAs+TBP) at 1.05 Torr. Figures 1(d) and 1(g) show the SEM images of two different $InAs_xP_{1-x}$ samples, grown using

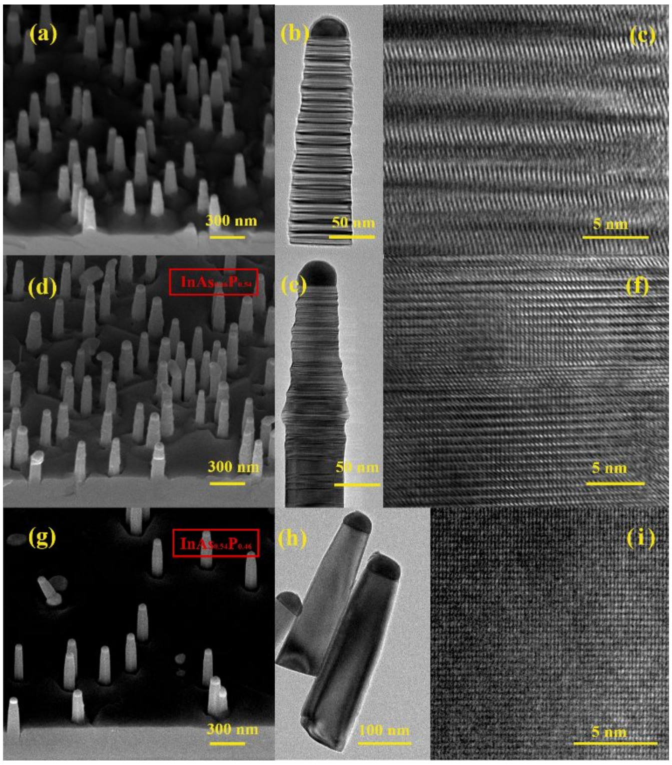

Figure 2 (a) 45°-tilted SEM image of InP NWs grown from 30 nm Au NPs, with the corresponding TEM image in panel (b) and HRTEM image in panel (c), respectively; (d) 45°-tilted SEM image of $InAs_{0.46}P_{0.54}$ NWs, with the corresponding TEM image in panel (e) and HRTEM images in panel (f), respectively; (g) 45°-titled SEM image of $InAs_{0.54}P_{0.46}$ NWs that exhibit pure WZ crystal phase, as demonstrated by the TEM image in panel (h) and the HRTEM image in panel (i).

TBAs and TBP line pressures of 0.10 Torr and 0.95 Torr, respectively (resulting in x=0.09), and 0.20 Torr and 0.85 Torr, respectively (resulting in x=0.36). TEM analysis of the first sample in Figures 1(e) and (f) reveals that stacking faults are still present in the $InAs_{0.09}P_{0.91}$ NWs, but their occurrence is reduced compared to InP NWs. Only ~36% of $InAs_{0.09}P_{0.91}$ NWs exhibit crystal defects. Instead, Figure 1 (h) shows a TEM image of the defect-free $InAs_{0.36}P_{0.64}$ WZ NW. The corresponding HRTEM image in panel (i) demonstrates the absence of any stacking faults. All NWs of this sample exhibit the defect-free WZ crystal phase. Therefore, higher fraction of InAs "x" in ternary $InAs_xP_{1-x}$ NWs grown from 20 nm Au NPs improves the crystal quality in the WZ phase. By comparing the SEM images of these samples, it is evident that the incorporation of As into the NWs leads to an increased radial growth, resulting in a more tapered NWs grown at the same temperature. This effect is likely due to the higher sticking coefficient of As compared to P[8], which enhances the nucleation probability on the NW sidewalls. Additionally, the average axial growth rate decreases monotonically with increasing the As fraction from 13 nm/min in pure InP NWs to 9 nm/min in $InAs_{0.36}P_{0.64}$ NWs.

Figure 2 presents the results of a similar study for NWs grown from Au NPs of 30 nm diameter. Additional TEM images are shown in section S2 of the supporting information. Panel (a) shows a 45°-tilted SEM image of an ensemble of binary InP NWs grown at the TMIn and TBP line pressures of 0.30 Torr and 0.40 Torr, respectively. As above, several V/III ratios were explored to identify the optimal growth conditions for binary InP NWs. However, in this case, the two distinct morphologies observed for 20 nm diameter colloids are not evident. The NWs appear highly defective in the entire range of TBP line pressures. Employing a TBP line pressure of 1.05 Torr, as for thinner NWs in Figure 1 (a), resulted in NWs with a high radial growth rate and limited elongation. Consequently, we decided to lower the TBP flux to 0.40 Torr, which gave nearly untapered NWs with negligible radial growth, as demonstrated in Figure 2 (a). Figures 2 (b) and (c) show the TEM and HRTEM images of a representative NW from this sample, where a high stacking fault density is clearly visible. The transition from a mixed ZB/WZ structure to pure WZ phase is observed for higher InAs fractions in NWs, as we saw earlier for 20 nm Au NPs. However, pure WZ phase requires a higher InAs fraction compared to 20 nm Au NPs. Figure 2(d) shows an ensemble of $InAs_{0.46}P_{0.54}$ NWs grown under TBAs and TBP line pressures of 0.15 Torr and 0.25 Torr, respectively. These NWs remain highly defective, as demonstrated by the representative TEM image in Figure 2 (e) and the corresponding HRTEM image in figure 2 (f). Defect-free WZ NWs shown in Figures 2(g) and (i) are grown under TBAs and TBP line pressures of 0.20 Torr and 0.20 Torr, respectively. This results in a higher InAs fraction of x=0.54, and does not lead to any significant change in either axial or radial growth rate. In contrast to the earlier suggestion[22], lower axial growth rates is not the only requirement for pure WZ phase in III-V NWs, at least in our case of ternary $InAs_xP_{1-x}$ NWs. It should be noted, however, that the increased InAs fraction results in a lower vertical yield of NWs, with a significant fraction of the NWs failing to nucleate. This can be seen in Figure 2 (g), where some catalyst NPs without any NWs are clearly visible on the substrate. This should be related to difficult nucleation of NWs on the substrate surface under the growth conditions that were chosen to obtain untapered NWs in pure WZ phase rather than maximize their yield.

It is clear at this point that the crystal phase of ternary $InAs_xP_{1-x}$ NWs strongly depends on the InAs fraction, with a critical composition x_c at which the structure transitions from highly defective to pure WZ. This critical composition increases with the NW diameter (or, equivalently, the Au NP diameter from which the NWs grow). Previous studies have speculated that defect formation in both InP and InAs binary NWs is related to the concentration of liquid In in the catalyst droplets[18,19] . Therefore, we performed the TEM-EDS measurements of the droplet compositions and contact angles for all the NWs discussed above. At least 20 NWs were investigated for each sample. These post-growth measurements were taken after cooling the samples in the absence of group V fluxes. This method has previously been demonstrated on binary NWs not to significantly alter the catalyst composition, providing an

Table 1 In and Au percentages and contact angles of the NPs on top of different $InAs_xP_{1-x}$ NWs

NP diameter (nm)	InAs fraction x	In (at%)	Au (at%)	Average contact angle (deg)
20	0	54 ± 2	46 ± 2	94 ± 5
20	0.09	52 ± 8	48 ± 8	87 ± 5
20	0.36	49 ± 3	51 ± 3	93 ± 3
30	0	65 ± 2	35 ± 2	84 ± 8
30	0.46	68.6±0.9	31.4±0.9	100 ± 5
30	0.54	65.3 ± 0.8	34.7±0.8	98 ± 3

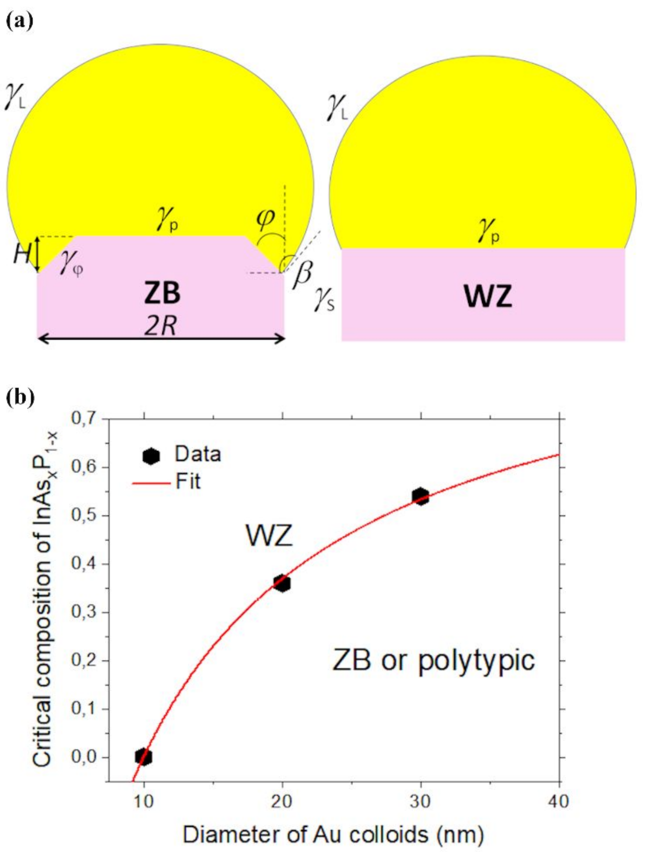

Figure 3 (a) Illustration of the truncated ZB and planar WZ growth interfaces under the catalyst droplet, showing the surface energies of interest. (b) Critical composition of InAs$_x$P$_{1-x}$ NWs x_c versus the Au nanoparticle diameter (symbols), fitted by Equation (6) at $x_c^\infty = 0.96$, $A = 5$ nm and $B = 3$ nm (line).

estimation of the catalyst composition during growth [23]. Here we used the same cooling procedure, so that we can compare the measured composition of the catalyst nanoparticles of the different samples after growth. The data in Table 1 show that the In/Au ratio inside the catalysts varies between 20 and 30 nm diameter samples. However, there is no significant change in the NP composition between binary InP and ternary InAs$_x$P$_{1-x}$ NWs. These results show that, unlike in the case of binary InP NWs[19], the crystal phase purity of ternary InAs$_x$P$_{1-x}$ NWs is not directly linked to the In content in the catalyst NPs (of course, both As and P atoms are not detected in the NPs due to their high volatility). Additionally, Table 1 shows no significant change in the average contact angle of the NPs on top of different NWs.

3. Modeling

To understand the composition and diameter-dependent polytypism and crystal phase purity of ternary InAs$_x$P$_{1-x}$ NWs under optimal conditions, we have developed the following energetic model. In the first approximation, we ignore the vapor-solid growth of tapered shells around the NW cores, thus assuming that the crystal phase is determined in the VLS growth step of the NW core. This was earlier justified for binary III-V NWs, where the tapered shells inherit the crystal phase of the VLS cores[24-27]. According to Refs. 26-31, the condition for the formation of VLS NWs in the WZ phase is equivalent to the preferred formation of vertical WZ facets relative to the truncated ZB facets:

$$\Delta\gamma = \frac{\gamma_\varphi}{\cos\varphi} - \gamma_P \tan\varphi - \gamma_S + \gamma_L \sin\beta > 0. \qquad (1)$$

Here, β is the droplet contact angle, φ is the angle of the truncated facet with respect to the vertical, γ_φ is the solid-liquid surface energy of the truncated facet, γ_P is the solid-liquid surface energy of horizontal facet under the droplet, γ_S is the solid-vapor surface energy of vertical WZ facet, and γ_L is the liquid-vapor surface energy of the droplet. The two solid-liquid surface energies γ_φ and γ_P are phase-independent[24,32]. Geometries of the NW tip and the interfaces of interest are illustrated in Figure 3(a). The surface energies γ entering Equation (1) are usually considered radius-independent[26-32]. This is valid for thick enough NWs with negligible contribution of the edges separating the side facets. For thin NWs, these edges start to play an important role in the total formation energy of hexahedral NWs[24,33-35]. The liquid surface and planar horizontal facet under the droplet have no edges, hence γ_L and γ_P are independent of the NW top radius (which is directly related to the nominal radius of Au colloids R).

Six equivalent facets of truncated ZB NWs and vertical WZ NWs are separated by edges. The surface energies γ per the surface area are $\sim RH$, with H as the truncation height (see Figure 3 (a)). Hence, the edge energies are inversely proportional to R. The total surface energies with the edge contributions are given by Ref. 24,34:

$$\gamma_\varphi = \Gamma_\varphi + \frac{\varepsilon_\varphi}{R},\ \gamma_S = \Gamma_S + \frac{\varepsilon_S}{R}. \qquad (2)$$

Here, Γ denotes the surface energy of flat facets and ε is the specific edge energy per unit length, with $\gamma_\varphi \to \Gamma_\varphi$ at large R. For InAs$_x$P$_{1-x}$ ternary NWs, the solid-vapor and liquid-vapor surface and edge energies depend on the composition x. The surface energies and edge energies of III-V ternary NWs in both ZB and WZ phases are unknown. Therefore, we use the simplest linear dependence on the composition in the first approximation[1,13]:

$$\Gamma_\varphi = \Gamma_\varphi^0(1 - c_\varphi^\Gamma x),\ \varepsilon_\varphi = \varepsilon_\varphi^0(1 - c_\varphi^\varepsilon x),$$
$$\Gamma_S = \Gamma_S^0(1 - c_S^\Gamma x),\ \varepsilon_S = \varepsilon_S^0(1 - c_S^\varepsilon x),$$
$$\gamma_P = \gamma_P^0(1 - c_P x). \qquad (3)$$

Here, the surface and edge energies labelled "0" correspond to pure InP NWs, and $x-$independent coefficients c describe linear interpolation of the surface and edge energies between pure InP and InAs. According to the calculations of Ref. 37, the vapor-solid surface energy Γ_S^0 of unpassivated vertical WZ facets $(1\bar{1}00)$ and $(11\bar{2}0)$ at zero temperature are 23.5% lower for InAs NWs, corresponding to positive $c_S^\Gamma = 0.235$. This corresponds to the well-known trend of having stable WZ phase in binary InAs NWs, where the ZB stacking is the exception rather than the rule[12,13]. Nothing is known about the edge energies of ternary NWs and the solid-liquid surface energies Γ_φ and γ_P, which is why the other coefficients c in Equations (3) can be of either signs.

The surface energy of liquid droplet should be independent of negligibly small concentrations of P and As atoms and even on the Au concentration, because the lower surface energy liquid In accumulates at the droplet surface[28-30]. The droplet contact angle β is the only kinetic parameter entering Eq. (1). It generally depends on the total V/III ratio and As/P flux ratio (and hence the composition x) due to kinetic growth effects[23]. We use linear interpolation of $sin\beta$ in Equation (1) of the form

$sin\beta(x) \cong sin\beta_0 + (cos\beta_0)c_\beta x$, with a coefficient c_β, and β_0 as the average contact angle of the droplets on top of pure InP NWs. This assumes a small variation of the contact angle compared to β_0. Post-growth measurements (see Table 1) show that the average contact angle of all the NWs is only slightly above 90°. In this case, the composition dependence of the contact angle is very weak, but this is not critical for our semi-quantitative model.

Using Equations (2) and (3) in Equation (1), we obtain the condition of the preferred WZ phase formation in the form $\Delta\gamma(R,x) > 0$. This allows us to find the critical composition x_c corresponding to the ZB-to-WZ phase transition as a function of the radius R. After some manipulations, Equation (1) can be put in the form

$$\Delta\gamma_0 - \frac{a}{R} + \left(d + \frac{b}{R}\right)x > 0, \quad (4)$$

with

$$\Delta\gamma_0 = \frac{\Gamma_\varphi^0}{cos\,\varphi} - \gamma_P^0 \tan\varphi - \Gamma_S^0 + \gamma_L \sin\beta_0,$$

$$a = \varepsilon_S^0 - \frac{\varepsilon_\varphi^0}{cos\varphi},$$

$$b = \varepsilon_S^0 c_S^\varepsilon - \frac{\varepsilon_\varphi^0 c_\varphi^\varepsilon}{cos\varphi},$$

$$d = \Gamma_S^0 c_S^\Gamma + \gamma_P^0 c_P tan\varphi + \gamma_L (cos\beta_0) c_\beta - \frac{\Gamma_\varphi^0 c_\varphi^\Gamma}{cos\,\varphi}. \quad (5)$$

Clearly, $\Delta\gamma_0$ is the surface energy difference that determines the crystal phase of thick InP NWs at a contact angle β_0, a/R is the composition-independent edge contribution, and the x term contains two contributions from the surface (d) and edge (b/r) energies. The WZ phase is energetically preferred when

$$x > x_c = x_c^\infty \frac{R-A}{R+B}, \quad (6)$$

with

$$x_c^\infty = -\frac{\Delta\gamma_0}{d}, A = \frac{a}{\Delta\gamma_0}, B = \frac{b}{d}. \quad (7)$$

The parameters x_c^∞, A and B lump together the largely unknown energetic factors influencing the crystal phase trend in thin III-V ternary NWs, and yield simple analytic shape of the critical curve $x_c(R)$. For x below the critical curve $x_c(R)$, the crystal phase can be polytypic rather than pure ZB due to a periodically changing geometry of the growth interface[26,30].

Our model describes different crystal phase trends depending on the sings and magnitudes of the coefficients entering Equation (6). The data shown in Figure 3(b) demonstrate that pure WZ phase of $InAs_xP_{1-x}$ grown in our experiments requires higher fractions of InAs for larger radii. The first data point in Figure 3 (b) corresponds to WZ InP NWs at $R = 5$ nm[19], which requires $A = 5$ nm in Equation (6). Monotonically increasing dependence $x_c(R)$ in the investigated range of NW compositions and Au radii requires positive x_c^∞ and positive A. From Equations (7), this corresponds to differently signed coefficients $\Delta\gamma_0$ and d, and equally signed coefficients $\Delta\gamma_0$ and a ($\Delta\gamma_0 > 0$, $a > 0$ and $d < 0$, or $\Delta\gamma_0 < 0$, $a < 0$ and $d > 0$). The sign of B in Equation (6) is less important. For example, the data points can reasonably be fitted by $x_c = x_c^\infty(1 - A/R)$ at $B \cong 0$. The fit shown in Figure 3 (b) is obtained with $x_c^\infty = 0.96$, $A = 5$ nm and $B = 3$ nm. This corresponds to pure WZ phase of very thin InP NWs ($R \leq 5$ nm), ZB or polytypic phase of thicker InP NWs, and almost pure WZ phase of thick InAs NWs under our growth conditions. The trend of a more stable WZ phase of InAs NWs relative to InP and all other binary III-V NWs is well-known and has been reproduced by different epitaxy techniques[24,38].

Experimental details

View Article Online
DOI: 10.1039/D5NR02409A

The NW samples in this work are epitaxially grown by means of Au-assisted VLS growth in a Riber C-21 chemical beam epitaxy (CBE) system. Trimethylindium (TMIn), pre-cracked tert-butyl arsine (TBAs) and tert-butyl phosphine (TBP) are used as gaseous metal–organic precursors, for which it is possible to measure the line pressures as a reference for the fluxes introduced into the chamber. The substrate temperature is measured with a pyrometer, providing an accuracy of ±10 °C. Prior to the mounting of the substrate in the reactor chamber, Au catalyst nanoparticles are deposited through colloids dispersion. Commercial water solutions of Au colloids with a nominal diameter of 20 nm and 30 nm (BBInternational EM.GCnn) are employed. Fe-doped InP(111)B substrates are first functionalized by wetting the surface through drop casting of 0.1% poly-l-lysine solution for 30s, then rinsed in deionized water and blown dried under N2 flux. The colloid solution is drop casted on the substrate surface, which is then rinsed in DI water and blown dried. Before inserting the sample in the growth chamber, the substrate is outgassed at 300°C on a heating stage for around five minutes, to get rid of the moisture. After the growth, the sample are imaged employing scanning electron microscopy (Zeiss Merlin SEM) operating at 5kV, from both top and side view, to check the NWs morphology and the ternary alloy composition of the NWs is measured through energy-dispersive X-ray analysis (EDS) employing a Bruker Quantax EDS system mounted on a Zeiss Ultraplus scanning electron microscope. Transmission electron microscopy (TEM), scanning transmission electron microscopy (STEM) and STEM–EDS of the catalyst nanoparticles were performed using a JEOL JEM-F200 Multipurpose microscope, working at 200 kV and equipped with a Schottky field-emission gun and a silicon-drift detector. TEM images were recorded with a GATAN RIO16 CMOS camera. The crystal structure of 20 NWs per sample is analyzed by TEM for statistical purposes. The percentage of defected NWs is calculated by counting the number of NWs in which stacking faults are observed, regardless of their density and distribution along the growth axis, over the total number of NWs measured.

4. Conclusions

In summary, we have demonstrated Au-catalyzed $InAs_xP_{1-x}$ NWs in pure WZ crystal phase for high enough fractions of InAs in the ternary alloy. The critical composition x_c for the formation of pure WZ phase in ternary NWs increases from 0.36 for 20 nm diameter to 0.54 for 30 nm diameter Au nanoparticles, and is expected to increase further for larger diameters. While a more predominant WZ phase in binary InAs NWs relative to InP NWs has been known, the composition and diameter dependent crystal phase purity of Au-catalyzed VLS ternary $InAs_xP_{1-x}$ NWs with small diameters has been studied here for the first time to our knowledge. The developed model explains the data on surface energetic grounds, where the effective surface energies vary with the NW composition, and the diameter dependence is due to the edge contributions into the overall energy balance. More advanced study should include kinetic contributions to the phase purity of III-V ternary NWs. These obtained results call for further systematic investigations of the crystal phase transitions in $InAs_xP_{1-x}$ NWs in a wider range of growth condition and Au nanoparticle

diameters, and similar investigations for other III-V ternary NWs grown by different methods.

Author contributions: G.B., V.Z. and L.S. have performed the growth of the NWs; G.B. has performed the TEM measurements; V.G.D. did the modeling part; F.B. have contributed to writing, review and editing. All authors have read and agreed to the published version of the manuscript.

Conflicts of interest

There are no conflicts to declare.

Data availability

The authors confirm that the data supporting the findings of this study are available within the article.

Acknowledgements

G.B., V.Z. and L.S. acknowledge the Center for Instrument Sharing of the University of Pisa (CISUP) for the TEM facilities and Prof. Enrico Mugnaioli and Dr. Michele Alderighi for the help during the TEM measurement sessions. This research was funded by Horizon EIC-PATHFINDEROPEN-01-01 QCEED (n. 101185617) and PNRR MUR project PE0000023-NQSTI projects. VGD acknowledges St.-Petersburg State University for the research project No. 129360164.

References

1 J. Johansson and K. A. Dick, *Cryst. Eng. Comm.*, 2011, **13**, 7175.
2 P. Caroff, J. Bolinsson and J. Johansson, *IEEE Journal on Selected Topics in Quantum Electronics*, 2011, **17**, 829–846.
3 R. Singh and G. Bester, *Phys Rev Lett*, 2009, **103**, 063601.
4 B. C. da Silva, O. D. D. Couto, H. T. Obata, M. M. de Lima, F. D. Bonani, C. E. de Oliveira, G. M. Sipahi, F. Iikawa and M. A. Cotta, *Sci Rep*, 2020, **10**, 7904
5 S. Assali, J. Greil, I. Zardo, A. Belabbes, M. W. A. De Moor, S. Koelling, P. M. Koenraad, F. Bechstedt, E. P. A. M. Bakkers and J. E. M. Haverkort, *J Appl Phys*, **120**, 044304
6 I. Kim, H. S. Kim and H. Ryu, *Molecules*, 2019, **24**, 3249
7 J. Liu, H. Yang, V. Khayrudinov, H. Lipsanen, H. Nie, K. Yang, B. Zhang and J. He, *Photonics Res*, 2021, **9**, 1811-1819
8 A. I. Persson, M. T. Björk, S. Jeppesen, J. B. Wagner, L. R. Wallenberg and L. Samuelson, *Nano Lett*, 2006, **6**, 403–407.
9 D. Dalacu, P. J. Poole and R. L. Williams, *Nanotechnology*, 2019, **30**, 232001.
10 G. Bucci, V. Zannier, F. Rossi, A. Musiał, J. Boniecki, G. Sęk and L. Sorba, *ACS Appl Mater Interfaces*, 2024, **16**, 26491–26499.
11 S. Haffouz, P. J. Poole, J. Jin, X. Wu, L. Ginet, K. Mnaymneh, D. Dalacu and R. L. Williams, *Appl Phys Lett*, 2020, **117**, 113102
12 V.G. Dubrovskii, *J. Phys. D: Appl. Phys.*, 2017, **50**, 453001
13 M. Ghasemi, E. D. Leshchenko and J. Johansson, *Nanotechnology*, 2021, **32**, 072001
14 K. A. Dick, C. Thelander, L. Samuelson and P. Caroff, *Nano Lett.*, 2010, **10**, 9, 3494–3499
15 M. E. Reimer, G. Bulgarini, A. Fognini, R. W. Heeres, B. J. Witek, M. A. M. Versteegh, A. Rubino, T. Braun, M. Kamp, S. Höfling, D. Dalacu, J. Lapointe, P. J. Poole and V. Zwiller, *Phys Rev B*, 2016, **93**, 195316
16 D. Dalacu, K. Mnaymneh, J. Lapointe, X. Wu, P. J. Poole, G. Bulgarini, V. Zwiller and M. E. Reimer, *Nano Lett*, 2012, **12**, 11, 5919–5923
17 T. Chiaramonte, L. H. G. Tizei, D. Ugarte and M. A. Cotta, *Nano Lett*, 2011, **11**, 5, 1934–1940
18 J. Johansson, K. A. Dick, P. Caroff, M. E. Messing, J. Bolinsson, K. Deppert and L. Samuelson, *The Journal of Physical Chemistry C*, 2010, **114**, 9, 3837–3842
19 F. Wang, C. Wang, Y. Wang, M. Zhang, Z. Han, S. Yip, L. Shen, N. Han, E. Y. B. Pun and J. C. Ho, *Sci Rep*, 2016, **6**, 32910
20 S. Lehmann, J. Wallentin, D. Jacobsson, K. Deppert and K. A. Dick, *Nano Lett*, 2013, **13**, 9, 4099–4105
21 S. Paiman, Q. Gao, H. H. Tan, C. Jagadish, X. Zhang and J. Zou, *J Cryst Growth*, 2013, **383**, 100–105
22 P. J. Poole, D. Dalacu, X. Wu, J. Lapointe and K. Mnaymneh, *Nanotechnology*, 2012, **23**, 385205
23 V. Zannier, F. Rossi, V. G. Dubrovskii, D. Ercolani, S. Battiato and L. Sorba, *Nano Lett*, 2018, **18**, 1, 167–174
24 V. G. Dubrovskii, *Nucleation theory and growth of nanostructures* (Springer, Heidelberg – New York – Dordrecht – London, 2014).
25 V.G. Dubrovskii, N.V. Sibirev, X. Zhang, and R. A. Suris, *Cryst. Growth Des.*, 2010, **10**, 3949
26 C. Y. Wen, J. Tersoff, K. Hillerich, M. C. Reuter, J. H. Park, S. Kodambaka, E. A. Stach and F. M. Ross, *Phys. Rev. Lett*. 2011, **107**, 025503
27 D. Jacobsson, F. Panciera, J. Tersoff, M. C. Reuter, S. Lehmann, S. Hofmann, K. A. Dick and F. M. Ross, *Nature* 2016, **531**, 317 (2016)
28 V. G. Dubrovskii, *Cryst. Growth Des*. 2017, **17**, 2544
29 V. G. Dubrovskii, N. V. Sibirev, N. N. Halder and D. Ritter, *J. Phys. Chem. C* 2019, **123**, 18693
30 F. Panciera, Z. Baraissov, G. Patriarche, V. G. Dubrovskii, F. Glas, L. Travers, U. Mirsaidov and J. C. Harmand, *Nano Lett*. 2020, **20**, 1669
31 V. G. Dubrovskii and F. Glas, *Cryst. Growth Des*. 2024, **24**, 9660
32 F. Glas, J. C. Harmand and G. Patriarche, *Phys. Rev. Lett*. 2007, **99**, 146101
33 T. Akiyama, K. Sano, K. Nakamura and T. Ito, *Jap. J. Appl. Phys*. 2006, **45**, L275
34 M. Rosini and R. Magri, *ACS Nano* 2010, **4**, 6021
35 V. Pankoke, P. Kratzer and S. Sakong, *Phys. Rev. B* 2011, **84**, 075455
36 E. D. Leshchenko and V. G. Dubrovskii, Nanomaterials 2023, **13**, 1659
37 N. V. Sibirev, M. A. Timofeeva, A. D. Bolshakov, M. V. Nazarenko and V. G. Dubrovskii, *Phys. Sol. State* 2010, **52**, 1531
38 K. A. Dick, P. Caroff, J. Bolinsson, M. E. Messing, J. Johansson, K. Deppert, L. R. Wallenberg and L. Samuelson, *Semicond. Sci. Technol*. 2010, **25**, 024009

The authors confirm that all data supporting the findings of this study are available within the manuscript.

View Article Online
DOI: 10.1039/D5NR02409A